Astron. Astrophys. 349, 169–176 (1999)

ASTRONOMY AND ASTROPHYSICS

Circumstellar matter around M-giants in symbiotic binaries: SY Muscae and RW Hydrae⋆

T. Dumm[1], **W. Schmutz**[1,2], **H. Schild**[1], **and H. Nussbaumer**[1]

[1] Institute of Astronomy, ETH-Zentrum, CH-8092 Zürich, Switzerland
[2] PMOD/WRC, CH-7260 Davos-Dorf, Switzerland

Received 28 May 1999 / Accepted 19 July 1999

Abstract. For the eclipsing symbiotic binary system SY Mus we present evidence for an asymmetric density distribution around the M-giant. We obtain this result from an improved orbital solution. We determine a revised orbital period of $P = 625.0 \pm 0.5$ d from UV eclipse observations and a re-analysis of the visual light curve. Based on new radial velocity observations, we measure the epoch of mid-eclipse accurately to within ± 6 days, or $1/100$ of the period. At ingress the eclipse curve is steeper and closer to mid-eclipse than at egress. From measured column densities of neutral hydrogen during egress we conclude that the mass loss rate of the M-giant is of the order of $\dot{M} \approx 5 \cdot 10^{-7}\ \mathrm{M}_\odot/\mathrm{yr}$.

The eclipse of the UV light in SY Mus and RW Hya can be partially explained by Rayleigh scattering but there is also an additional source of opacity. HST high resolution UV observations of RW Hya during egress reveal that this additional flux attenuation is due to blanketing by numerous absorption lines, predominantly Fe II. Line blanketing is an important effect that has to be taken into account to explain the eclipse of SY Mus and of other symbiotic binaries.

Key words: stars: circumstellar matter – stars: binaries: symbiotic – stars: late-type – stars: mass-loss – stars: individual: SY Mus – stars: individual: RW Hya

1. Introduction

Mass loss is of central importance in stellar evolution. For intermediate and low mass stars mass-loss becomes significant when they enter the red giant phase (Schaller et al. 1992). Theoretically, mass loss from M giants is not yet understood. An important factor that hampers the development of theoretical models is the paucity of observational constraints as to what is driving the winds of M giants. The empirical determination of their wind structure is therefore fundamental.

Vogel (1991), Vogel et al. (1992), and Pereira et al. (1999) analyzed the M-giant wind in the eclipsing symbiotic systems EG And and SY Mus. In these systems, a hot radiation source probes the column density of neutral hydrogen of the wind from the red giant due to the Rayleigh scattering effect. Assuming spherical symmetry for the mass loss, $\dot{M}$, they derived empirically the velocity structure of the wind of the M giant.

In this paper we draw attention to two complicating factors which have been neglected so far in this type of analysis. Based on a new orbital solution of SY Mus (Sect. 3) we show that the UV eclipse curve is not symmetric with respect to mid-eclipse. We investigate the density structure and derive the mass-loss rate of the red giant (Sect. 4). We then use HST spectra of RW Hya and demonstrate, that in addition to Rayleigh scattering, an important source of absorption is due to line blanketing (Sect. 5).

2. Observations

2.1. Optical high resolution spectra of SY Mus

SY Mus was observed with the Coudé échelle spectrograph (CES) fed by the 1.4 m Coudé auxiliary telescope (CAT) at the European Southern Observatory. The spectra have a resolution of $R \approx 60\,000$, and cover ≈ 60 Å. The spectra are centered at 4363 Å, 5007 Å, 6563 Å, 6825 Å , or 7005 Å . In these settings M-giants have numerous absorption lines. Radial velocities (RV) of the M-star in SY Mus were determined by cross correlation with the radial velocity standard HR 4763 ($v_0 = 21.3 \pm 0.1\ \mathrm{km\,s^{-1}}$, Foster & Wall 1998). The radial velocities are given in Table 1. Measurements during the same observing nights have been averaged. This results in a total of 30 data points. We combine our measurements with the RV-data in Table 1 of Schmutz et al. (1994).

2.2. IUE low resolution spectra of SY Mus

In the last IUE observing cycle we covered with the key program SI067, the egress phase of SY Mus with the goal of deriving the velocity law for the late giant in the system. Including these observations, the final IUE archive contains 69 short wavelength, low resolution spectra of SY Mus. In this paper we analyze 44

Send offprint requests to: T. Dumm

⋆ Based on observations made with IUE, HST and at the European Southern Observatory at La Silla (Chile). ESO observations were granted for the proposals 47.7-081, 48.7-083, 49.7-041, 50.7-129, 51.7-093, 52.7-068, 53.7-083, 54.E-061, 55.E-446, 56.E-526 57.D-684, 58.D-248, 59.D-700, 60.D-714. The visual brightness estimates were done by the RASNZ.

Table 1. Radial velocity data of SY Mus. Given are the Julian date, the orbital phase according to Eq. 1 and the radial velocity of the M-giant.

JD	ϕ	v_r [km/s]	JD	ϕ	v_r [km/s]
2449368	0.71	6.13	2450287	0.18	21.01
2449725	0.28	20.54	2450304	0.20	21.39
2449811	0.42	17.01	2450483	0.49	13.56
2450149	0.96	9.91	2450500	0.52	11.86
2450173	0.00	12.96	2450515	0.54	10.47
2450188	0.02	13.47	2450531	0.57	8.93
2450202	0.04	14.42	2450559	0.61	7.16
2450210	0.05	15.05	2450591	0.66	6.40
2450221	0.07	16.69	2450650	0.76	5.06
2450237	0.10	18.64	2450825	0.04	14.79
2450267	0.15	18.06			

SWP low resolution spectra with a signal to noise ratio better than 4 at 1600 Å.

Short-ward of 1600 Å the hot component dominates the continuum at all orbital phases. We measured the continuum flux at the two wavelengths 1325 Å and 1600 Å, which are free from strong emission lines. The values are listed in Table 2.

2.3. HST UV spectra of RW Hya

The eclipsing symbiotic binary system RW Hya has been observed during three visits with the Goddard High Resolution Spectrograph (GHRS) on board HST in cycles 5 and 6. We used the gratings G140L and G140M which provide resolutions of $R \approx 2\,000$ and $R \approx 20\,000$, respectively. In Table 3 we list the observing dates and exposure times of the GHRS observations. The observations on JD 2 450 261 were during eclipse of the hot object by the red giant, the observations on JD 2 450 286 were during egress. The orbital phases are according to the ephemeris of Schild et al. (1996) and Kenyon & Mikolajewska (1995).

3. Orbit of SY Mus

3.1. Orbital period

Pereira et al. (1995) determined an orbital period of SY Mus based on about 2500 visual estimates by the observers of the Variable Section of the Royal Astronomical Society of New Zealand (RASNZ). Their data set covers ≈ 22 orbital cycles, and they derive a period of $P = 624.5 \pm 0.3$ days.

In Fig. 1 we show IUE UV light curves corresponding to periods $P = 624.0$, $P = 624.5$, $P = 625.0$ and $P = 625.2$ days. For all four curves, T_0 is set to the value derived in Sect. 3.2. The IUE SWP10188L spectrum is separated by 9 orbits from the spectra of similar phase. It is taken at ingress and shows already a heavily attenuated stellar continuum. In the light curve corresponding to $P = 624.5$, this spectrum is flanked by spectra showing almost no continuum attenuation (see Fig. 1). We find, that an orbital period of $P \geq 625.0$ days is required to obtain a continuous UV light curve. This is only $1.7\,\sigma$ larger than the value $P = 624.5 \pm 0.3$ days derived by Pereira et al. (1995).

Table 2. IUE low resolution short wavelength camera spectra of SY Mus. Given are the orbital phase ϕ according to Eq. 1, the Julian date, the SWP image number, and continuum fluxes at 1325 Å and 1600 Å in units of 10^{-13} erg cm^{-2} s^{-1} Å^{-1}.

ϕ	JD 2 400 000+	SWP	1325 Å	1600 Å
0.525	48629	43561	1.29	1.25
0.621	44939	15594	1.20	1.16
0.638	44950	15705	1.08	1.03
0.675	48723	44366	1.09	1.01
0.675	48723	44367	0.93	1.23
0.693	48109	39404	1.16	1.04
0.750	45020	16381	1.06	1.00
0.899	48863	45461	0.95	0.66
0.899	49488	50768	0.89	0.69
0.910	50120	56762	0.92	0.73
0.917	49499	50897	0.84	0.67
0.923	50128	56805	0.61	0.55
0.923	44503	10188	0.12	0.40
0.931	49508	51007	0.08	0.34
0.938	50137	56846	0.14	0.42
0.950	48270	40583	0.11	0.13
1.018	50187	56974	0.12	0.16
1.053	45834	23011	0.12	0.17
1.054	47710	36597	0.11	0.13
1.085	50229	57250	0.12	0.27
1.096	50236	57315	0.16	0.30
1.101	50239	57336	0.14	0.41
1.102	48365	41417	0.25	0.47
1.106	50242	57357	0.26	0.49
1.112	50246	57388	0.36	0.49
1.123	50253	57418	0.39	0.43
1.131	50258	57438	0.47	0.58
1.154	50272	57503	0.89	0.73
1.163	47778	36965	0.94	0.84
1.170	50282	57551	1.00	0.84
1.240	48451	42056	1.00	0.96
1.240	48451	42057	0.89	0.83
1.275	48473	42172	1.03	0.97
1.275	48473	42171	1.12	0.98
1.285	48479	42208	1.06	0.90
1.285	48479	42207	1.12	1.03
1.309	48494	42320	1.16	1.10
1.309	48494	42321	0.96	0.99
1.328	47881	37856	1.27	1.04
1.328	47881	37855	0.91	1.04
1.346	44767	14238	1.14	1.11
1.346	44767	14237	1.11	1.04
1.480	47976	38436	1.45	1.24
1.480	47976	38437	1.14	1.02

The upper limit for the period inferred by the UV light curve is $P \leq 628.0$ days.

The visual estimates of SY Mus do not show any erratic variability. The mean visual magnitude 11.022 ± 0.004 of the light curve also remained stable during 40 years (Pereira et al. 1995). Different atmospheric extensions due to stellar pulsations are

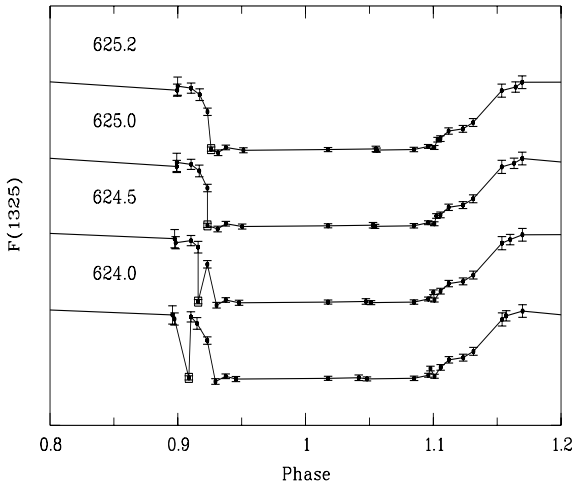

Fig. 1. Continuum flux at 1325 Å versus phase. The four light curves correspond to 4 different orbital periods: $P = 624.0, 624.5, 625.0$ and 625.2 days. The obscuration of JD 2 444 503 (SWP10188L) is marked with a square.

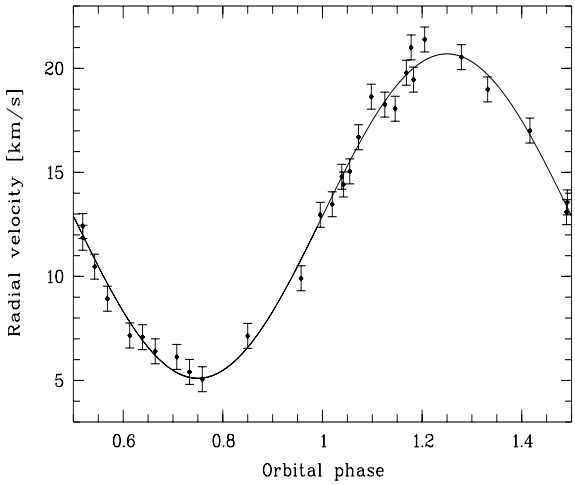

Fig. 2. Radial velocity data of SY Mus derived from optical high resolution spectra, compared with the circular solution from Tab 4.

Table 3. HST GHRS observing log of RW Hya. Exposure times are given in seconds. Orbital phases are according to the ephemeris of Schild et al. (1996)

Julian date [24+]		50 148	50 261	50 286
Phase ϕ		0.72	0.02	0.09
Grating	Range [Å]			
G140L	1170–1460	2×218	762	435
G140L	1480–1760	2×218	653	435
G140M	1226–1254	435	1414	544
G140M	1386–1414	435	1197	340
G140M	1470–1498	1197	1197	–
G140M	1536–1563	–	1183	435
G140M	1627–1654	–	1414	544

Table 4. Orbital parameters of the M star in SY Mus. T_0 gives the Julian date when the M-giant is in front of the white dwarf. For the eccentric solution $T_{\rm P}$ gives the time of periastron passage.

Parameter	Old[1]	Eccentric	Circular	Adopted
P [d]	624.5	624.1	624.7	625.0[2]
$T_{\rm P}$ [24+]	-	50156	-	-
T_0 [24+]	50175	50174	50 176	50 176
V_0 [km/s]	12.9	12.9	12.9	12.9
K [km/s]	7.4	7.8	7.8	7.8
ε	0	0.03	0	0
ω [°]	-	349	-	-
$< O-C >$ [km/s]		0.54	0.56	0.57

[1] from Schmutz et al. (1994)
[2] see Sect. 3.1

therefore unlikely to be the cause for the attenuation in the SWP10188L spectrum.

We also analyzed the updated time series of the visual estimates kindly provided by the RASNZ. Our sample has been collected in the years 1954-1999 and covers 26 orbits, which is 4 orbits more than has been analyzed by Pereira et al. (1995). The number of measurements increased from $\approx 2\,500$ to 3 650. This is a significant improvement, as the amplitude of the variability is only 1.6 times the $1\,\sigma$ error of a single measurement. Based on the visual estimates, we derive a new photometric period of $P = 624.9 \pm 0.3$ days. The combination of $P \geq 625.0$ days and $P = 624.9 \pm 0.3$ days, leads us to adopt $P = 625$ days.

3.2. Radial velocity curve of the M-giant

In order to derive an accurate time of mid-eclipse for SY Mus, we perform a least squares fit including our new 21 RV-measurements and the 9 RV-measurements of Schmutz et al. (1994). This yields the orbital parameters listed in Table 4. The derived orbital periods for the eccentric and the circular solutions are in good agreement with a period of 625.0 days, as derived in Sect. 3.1. The orbital solutions are consistent with the previous analysis of Schmutz et al. (1994).

To test whether the eccentric solution is significantly better than the circular solution we compare the sum $M = \sum_{i=1}^{n}(O-C)_i^2/\sigma^2$ with the expected value $f = n - m$. The number of free parameters for the eccentric solution is $m = 6$, for the circular solution it is $m = 4$. The number of measurements is $n = 30$. The mean deviations $< (O-C) >$ listed in Table 4 indicate an observational error of the radial velocities of $\sigma = 0.6\,\mathrm{km\,s^{-1}}$. The eccentric solution is thus not significantly better than the circular solution. The circular solution and the radial velocity data are shown in Fig. 2. As the theory of tidal forces in binaries (Zahn 1977) also predicts the orbit to be circular, we will calculate the phase of a given date JD according to the circular fit with the period from Sect. 3.1:

$$\phi = (\mathrm{JD} - 2\,450\,176)/625.0. \quad (1)$$

To derive an error for the time of mid-eclipse, T_0, we have done a series of least squares fits, where for each fit the period was set to a value in the range $623.5 \ldots 626.5$ days. We find that fits where T_0 differs by more than 6 days from JD 2 450 176 lead to M-values outside the expected range $f \pm \sqrt{2f}$. The phases

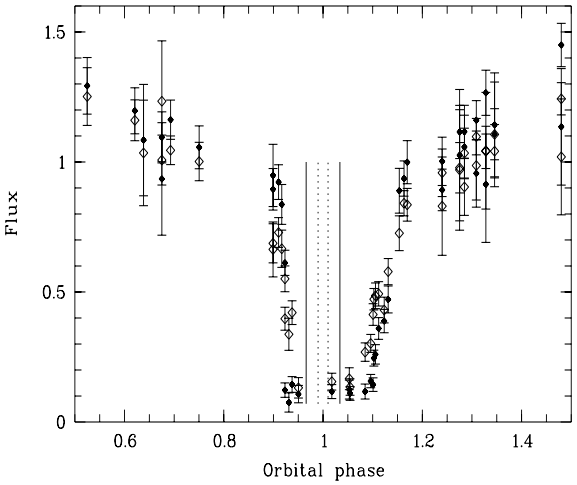

Fig. 3. Measured flux in SY Mus at 1325 Å (filled diamonds) and 1600 Å (open diamonds) as a function of orbital phase ϕ. Vertical lines delimit the phases of geometric eclipse (solid) and the uncertainty for the time of central eclipse $\Delta\phi = \pm 0.01$ (dotted). Flux in units of 10^{-13} erg cm^{-2} s^{-1} Å^{-1}.

of all attenuated IUE spectra in Table 2 (except SWP10188L) have an uncertainty $\Delta\phi \leq 0.01$.

4. Asymmetric eclipse curve of SY Mus

It is important to note that our time of mid-eclipse is not based on the light curve shape but on RV measurements. This is a crucial point because we intend to study asymmetries in the eclipse curve.

4.1. Column density of neutral hydrogen

During ingress and egress we observe attenuation at wavelengths < 1600 Å due to Rayleigh scattering and a second opacity source of up to now unknown origin. This second source of opacity has already been described in Pereira et al. (1995).

In Fig. 3, we show the continuum variation at 1325 Å and 1600 Å. At 1325 Å Rayleigh scattering efficiency is very high, getting smaller towards longer wavelengths. The eclipse curve is clearly asymmetric with respect to the phase of central eclipse. At ingress a sharp flux reduction starts at $\phi \approx 0.9$. The reappearance of the hot continuum is less steep and continues until approximately $\phi \approx 1.18$.

We determine the column densities of neutral hydrogen, $n_{\rm HI}$, with a similar approach as the one adopted by Pereira et al. (1995). We rewrite their Eq. 3

$$F_\lambda(\phi) = F_\lambda(\phi_0) \cdot e^{-\tau_{\rm A}(\phi) - n_{\rm HI}(\phi)\sigma_{\rm R}(\lambda)}. \quad (2)$$

The term $e^{-\tau_{\rm A}(\phi)}$ models an additional opacity source in a wavelength independent way, as the IUE low resolution spectra do not allow a more detailed approach. We use the spectrum SWP56762 observed at $\phi = 0.912$ as reference spectrum $F_\lambda(\phi_0)$. This spectrum does not yet show attenuation due to Rayleigh scattering. In addition it is least affected by nebular emission, as it is taken close to the onset of the eclipse.

Table 5. Column density of neutral hydrogen $n_{\rm HI}$ and the optical depth $e^{-\tau_{\rm A}}$ in SY Mus according to Eq. 2 as a function of orbital phase ϕ, and impact parameter b (in units of M-giant radii). The errors of $n_{\rm HI}$ are of the order of 50%.

ϕ	b [R$_{\rm r}$]	$n_{\rm HI}$ [cm^{-2}]	$e^{-\tau_{\rm A}}$
0.910	2.33	$< 1.0 \cdot 10^{21}$	-
0.917	2.18	$4.0 \cdot 10^{21}$	0.8
0.923	2.04	$4.0 \cdot 10^{22}$	0.7
0.923[1)]	2.04	$6.0 \cdot 10^{23}$	0.6
0.931	1.85	$8.0 \cdot 10^{23}$	0.6
0.938	1.68	$7.0 \cdot 10^{23}$	0.6
0.950	1.39	$> 1.0 \cdot 10^{25}$	-
1.018	0.65	$> 1.0 \cdot 10^{25}$	-
1.053	1.46	$> 1.0 \cdot 10^{25}$	-
1.054	1.49	$> 1.0 \cdot 10^{25}$	-
1.085	2.22	$1.5 \cdot 10^{24}$	0.4
1.096	2.47	$5.0 \cdot 10^{23}$	0.4
1.101	2.57	$3.0 \cdot 10^{23}$	0.4
1.102	2.59	$4.0 \cdot 10^{23}$	0.6
1.106	2.68	$2.5 \cdot 10^{23}$	0.6
1.112	2.80	$1.5 \cdot 10^{23}$	0.6
1.123	3.02	$1.5 \cdot 10^{23}$	0.6
1.131	3.17	$1.0 \cdot 10^{23}$	0.7
1.154	3.55	$5.0 \cdot 10^{21}$	1.0
1.163	3.68	$< 1.0 \cdot 10^{21}$	-

[1)] SWP10188L

By fitting the ingress and egress variation with Eq. 2, we derive the column densities $n_{\rm HI}$ and additional optical depths $\tau_{\rm A}$ (Table 5). The error in the derived column density of neutral hydrogen is estimated to be of the order of 50%. At low and high column densities the uncertainties tend to be even larger. This error does not include systematic effects due to line blanketing discussed in Sect. 5. For those IUE spectra we have in common with Pereira et al. (1999), we find agreement within the error bars. In Fig. 4 the column densities are plotted as a function of the impact parameter b, given by

$$b^2 = p^2(\cos^2 i + \sin^2 \phi \, \sin^2 i). \quad (3)$$

The orbital inclination of SY Mus is $i = 95.8 \pm 1.7°$ (Harries & Howarth 1996) and the stellar separation is $p = (2.6 \pm 0.2) \cdot 10^{13}$ cm, or in units of the M-giant radius $R_{\rm r} = 86\,{\rm R}_\odot$ (Schmutz et al. 1994) $p = (4.3 \pm 0.7)\,{\rm R_r}$.

Fig. 4 shows that the column density of neutral hydrogen in SY Mus is clearly asymmetric with respect to mid-eclipse.

4.2. Mass-loss rate and wind acceleration

Because the density distribution around SY Mus is not symmetric, we model the ingress and egress column densities separately with two independent, semi-spherically symmetric solutions for the volume density

$$N_{\rm H}(r) = \frac{4\pi\,\mu\,m_{\rm H}\,v_\infty\,v(r)}{\dot{M}}, \quad (4)$$

where $\dot{M}$ is the mass-loss rate of the M-giant, and $v(r)$ the velocity in units of the terminal velocity v_∞. For a neutral wind

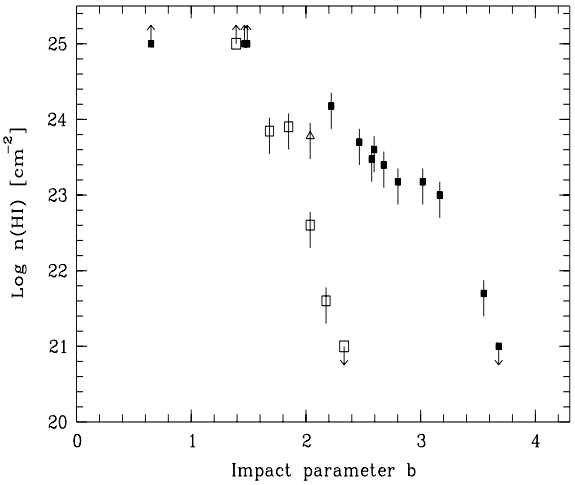

Fig. 4. Column density of neutral hydrogen in SY Mus as a function of impact parameter b, open squares ingress data, solid squares egress data. Upper and lower limits are indicated by arrows. b in units of M-giant radii. The triangle marks the column density derived from the SWP10188L spectrum, for which the phase relative to the other observations depends on the adopted period.

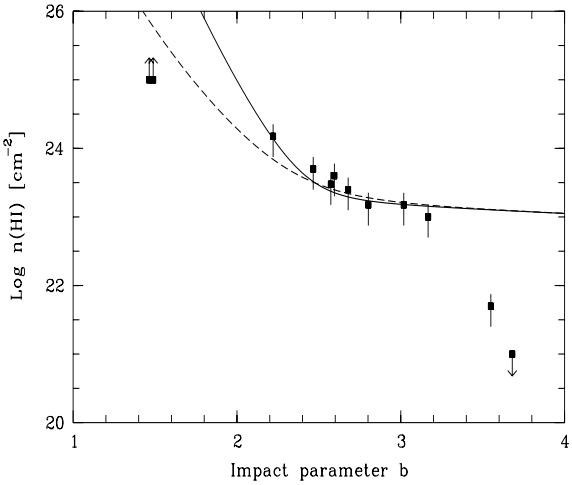

Fig. 5. Column density of neutral hydrogen during egress. The solid line gives the fit according to Eq. 10, with the fit parameters $\dot{M} = 5 \cdot 10^{-7}$ M$_\odot$, $v_\infty = 20$ km s^{-1}, $k = 20$, $a_\mathrm{k} = 1 \cdot 10^{31}$ cm^{-2}, the dashed line belongs to $k = 12$, $a_\mathrm{k} = 7 \cdot 10^{27}$ cm^{-2}.

which consists mainly of hydrogen, the mean atomic weight is $\mu \approx 1$. The total column density of hydrogen along the line of sight l is then given by

$$n_\mathrm{H}(b \geq 1) = \int_{-\infty}^{\infty} N_\mathrm{H}(r)\, dl = a \cdot \int_b^{\infty} \frac{dr}{r\, v(r) \sqrt{r^2 - b^2}}, \quad (5)$$

where b and r are in units of the M-giant radius R_r. The parameter a is defined by

$$a = \frac{2\dot{M}}{4\pi\, \mu\, m_\mathrm{H}\, v_\infty\, R_\mathrm{r}}. \quad (6)$$

We want to solve Eq. 5 for the velocity law $v(r)$. According to Knill et al. (1993), it is particularly advantageous to expand the function $n_\mathrm{H}(b)$ into a Taylor series

$$n_\mathrm{H}(b) = \sum_{k=1}^{\infty} \frac{a_\mathrm{k}}{b^k}, \quad (7)$$

as the velocity law, $v(r)$, is then given by

$$\frac{a}{r\, v(r)} = \sum_{k=1}^{\infty} \frac{a_\mathrm{k}}{\lambda_\mathrm{k} r^k}, \quad (8)$$

with the constants λ_k recursively defined by

$$\lambda_1 = \pi/2 \qquad \lambda_\mathrm{k} \cdot \lambda_{\mathrm{k}-1} = \pi/(2k-2). \quad (9)$$

Due to the limited orbital coverage and limited precision of the column densities, a unique determination of the velocity profile is not possible. Therefore, we reduce Eq. 7 to the first term ($k = 1$) and one term of order $k > 1$. Thus we rewrite Eq. 7 into

$$n_\mathrm{H}(b) = \frac{a_1}{b} + \frac{a_\mathrm{k}}{b^k}, \quad (10)$$

and Eq. 8 reduces to

$$\frac{a}{r\, v(r)} = \frac{a_1}{\lambda_1 r} + \frac{a_\mathrm{k}}{\lambda_\mathrm{k} r^k}. \quad (11)$$

The factors a_1, a_k, and the exponent k in Eq. 11 are our fit parameters.

Eq. 10 requires that we know the total column density of hydrogen as a function of impact parameter b. In symbiotic binaries a fraction of the wind is ionized by the hot star. Thus the measured column densities of neutral hydrogen can be substantially smaller than the total column density of hydrogen.

During egress of SY Mus, there is a region around $b \approx 3$ R$_\mathrm{r}$ where $n_\mathrm{HI} \approx b^{-1}$ (see Fig. 5). From $b = 3.1$ R$_\mathrm{r}$ to $b = 3.6$ R$_\mathrm{r}$, there is a sudden drop in the column density of neutral hydrogen (see Fig. 5). In the following we model this behaviour by a wind that has reached terminal velocity at $b \approx 3$ R$_\mathrm{r}$, with $n_\mathrm{H} \approx 10^{23}$ cm^{-2}, and is substantially ionized at impact parameters $b \gtrsim 3.6$ R$_\mathrm{r}$. From the sudden decrease in column density we also deduce that the transition from mainly neutral to mainly ionized hydrogen is almost instantaneous. Thus, the amount of ionized material at $b \approx 3$ R$_\mathrm{r}$ is negligible, and our measured column density of neutral hydrogen n_HI at $b \lesssim 3.2$ R$_\mathrm{r}$ is close to the total column density of hydrogen n_H.

The first term in Eq. 10 and Eq. 11 is the dominant term for large b values, and corresponds to the solution of a stellar wind with constant expansion velocity v_∞, where the volume density is proportional to r^{-2}. A total column density of hydrogen of $n_\mathrm{H}(b) \approx 1.5 \cdot 10^{23}$ cm^{-2} at $b \approx 3$ R$_\mathrm{r}$, where the first term in Eq. 10 dominates, leads to

$$a_1 = n_\mathrm{H}(b) \cdot b \approx 4.5 \cdot 10^{23}\ \mathrm{cm}^{-2}, \quad (12)$$

which yields

$$a = 2\, a_1/\pi \approx 3 \cdot 10^{23}\ \mathrm{cm}^{-2}. \quad (13)$$

Typical terminal velocities v_∞ for M-giant winds from molecular absorption band analysis are in the range $10 -$

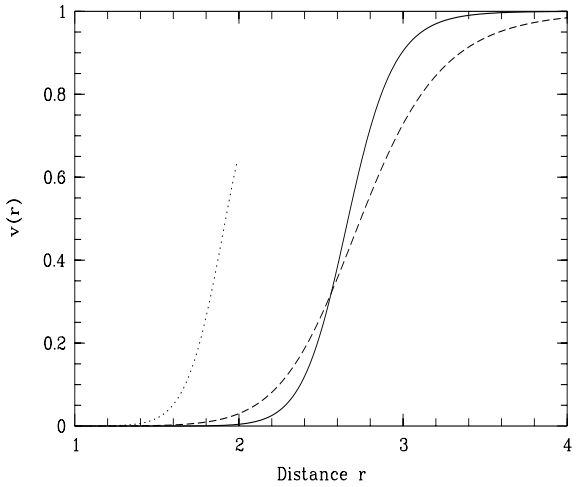

Fig. 6. Velocity profile as derived from egress data. The solid line gives the velocity law for $k = 20$, the dashed line for $k = 12$. The velocity is given in units of $v_\infty = 20\ \mathrm{km\,s^{-1}}$, the distance from the M-giant is given in units of the its radius R_r. The dotted line gives a possible wind solution for the ingress data.

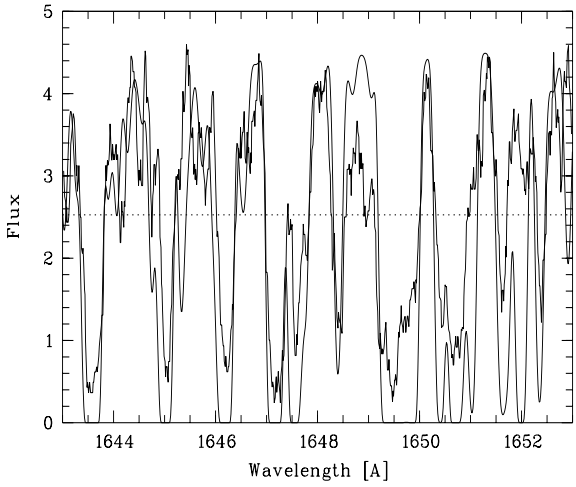

Fig. 7. Observed GHRS medium resolution spectrum of RW Hya at phase $\phi = 0.09$ (thick line) compared with a simple "absorption only" radiation transfer simulation (thin line). Most absorption features are due to Fe II. The dotted line gives the continuum as it would be seen in a IUE low resolution spectrum. Flux in units of 10^{-13} erg cm^{-2} s^{-1} Å^{-1}.

$30\ \mathrm{km\,s^{-1}}$. In the following we adopt $v_\infty = 20\ \mathrm{km\,s^{-1}}$ This implies a mass-loss rate for the M-giant in SY Mus of

$$\dot{M} = 2\pi\mu m_\mathrm{H}\, v_\infty\, \mathrm{R_r\, a} \approx 5 \cdot 10^{-7}\ \mathrm{M_\odot/yr}. \quad (14)$$

The second term in Eq. 10 and Eq. 11 is the dominant term for small impact parameters. It determines where the acceleration of the M-giant wind takes place. The best fit parameters for the second term in Eq. 10 are $k \approx 20$ and $a_\mathrm{k} \approx 1 \cdot 10^{31}\ \mathrm{cm^{-2}}$ (see Fig. 5). The resulting velocity profile is shown in Fig. 6.

If we assume, that for column densities $\lesssim 10^{23}\ \mathrm{cm^{-2}}$, ionization becomes significant, the ingress data does not allow to derive a mass-loss rate (see Fig. 4). Assuming the mass-loss rate derived from the egress data, we find $k \approx 12$ and $a_\mathrm{k} \approx 7 \cdot 10^{27}\ \mathrm{cm^{-2}}$, with large uncertainties. The wind acceleration then takes place at $\approx 2\ \mathrm{R_r}$ (see Fig. 6).

5. Line blanketing in RW Hya

So far Rayleigh scattering has been observed in the symbiotic systems EG And (Vogel 1991), SY Mus (Pereira et al. 1995), BF Cyg (Gonzalez-Riestra et al. 1990), and RW Hya (this paper). Only in the case of EG And is Rayleigh scattering sufficient to interpret the continuum attenuation. In the other cases there is clear evidence for additional absorption. This additional attenuation has been accounted for by a wavelength independent term of unknown origin (Gonzalez-Riestra et al. 1990, Pereira et al. 1995). Pereira et al. (1995) suggest, that the additional attenuation is produced by Thomson scattering by free electrons in the nebula. However, according to Schmid (1995), high electron densities of $n_\mathrm{e} > 10^{10}\ \mathrm{cm^{-3}}$ in the ionized region would be needed. Here, we put forward an alternative explanation: line blanketing due to mostly Fe II transitions. This "iron-curtain" has first been identified by Shore & Aufdenberg (1993) as the origin of the distorted emission lines and anomalous emission line ratios observed in symbiotic binaries. The iron curtain has also been observed in the spectrum of PU Vul (Schmutz et al. 1993). The iron absorption line forest is not resolved in IUE low resolution spectra, and could thus be the cause of the almost wavelength independent attenuation, observed during eclipse in SY Mus. There are no IUE high resolution spectra of SY Mus during ingress or egress.

As RW Hya and SY Mus show very similar observational characteristics (Schmutz et al. 1994, Schild et al. 1996) we analyze HST GHRS spectra of RW Hya to investigate the origin of the additional continuum attenuation in SY Mus.

In Fig. 7 we show an extract of 10 Å of the HST spectra of RW Hya taken at egress phase. In this wavelength region, the continuum is dominated by the hot star. It is distorted by numerous Fe II absorption lines. These lines are only seen during the ingress and egress phases and they have their origin in the extended atmosphere or wind of the red giant. These lines require high spectral resolution to be resolved, and it is therefore impossible to measure correctly the absorption due to Rayleigh scattering with IUE low resolution spectra. IUE final archive low resolution short wavelength spectra taken through the large aperture have a resolution of 5 Å. In the presence of numerous absorption lines, this leads to a significant underestimation of the stellar continuum. In Fig. 7 we have marked the continuum level that would be seen in an IUE low resolution spectrum, which is at about half of the true continuum value.

We have fitted HST spectra of RW Hya with a simple plane–parallel "absorption only" radiation transfer model where the level populations of the transitions are calculated in LTE. The input parameters were: a radiation temperature of $T_\mathrm{r} = 3\,800\,\mathrm{K}$, an electron temperature of $T_\mathrm{e} = 10\,000\ \mathrm{K}$, micro-turbulence of $v_\mathrm{D} = 13\ \mathrm{km\,s^{-1}}$, an ion density of $N_\mathrm{i} = 3 \cdot 10^8\ \mathrm{cm^{-3}}$, solar iron abundance and the thickness of the absorbing layer corresponding to $l = 10^{14}\ \mathrm{cm}$. The electron temperature is in

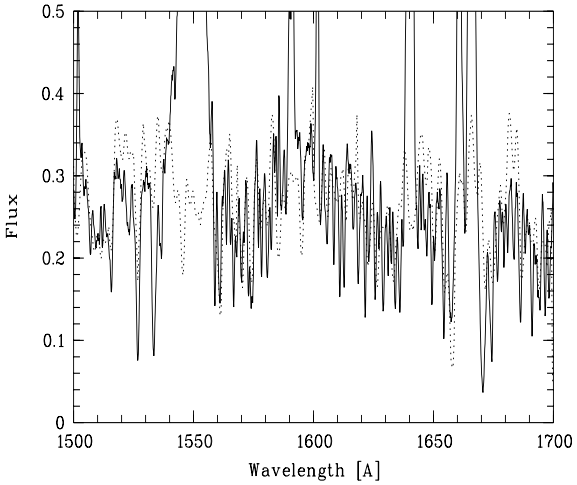

Fig. 8. HST low resolution spectra of RW Hya at $\phi = 0.09$ (solid) together with the "absorption only" radiation transfer simulation (dotted). Flux in units of 10^{-13} erg cm^{-2} s^{-1} Å^{-1}.

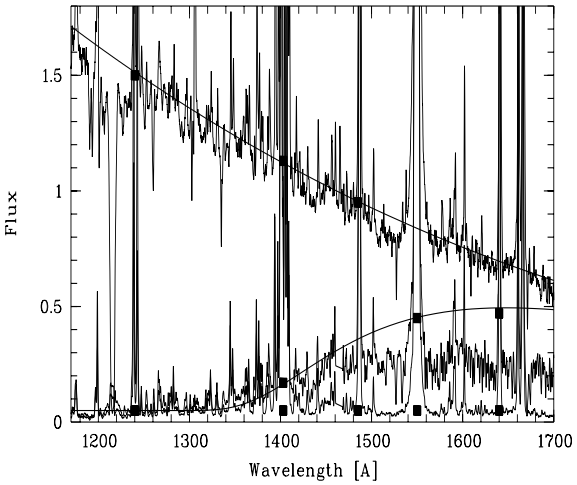

Fig. 9. HST low resolution spectra of RW Hya at $\phi = 0.72$, $\phi = 0.09$ and $\phi = 0.02$ (top to bottom). We also mark the continuum values derived from the HST medium resolution spectra taken at $\phi = 0.72$ and $\phi = 0.09$ (filled squares). Also shown is a Planck function belonging to 100 000 K, with and without Rayleigh scattering on $1.5 \cdot 10^{24}$ cm^{-2}. Flux in units of 10^{-13} erg cm^{-2} s^{-1} Å^{-1}.

the range predicted by the models of Schwank et al. (1997). The resulting fit is shown in Fig. 7 and Fig. 8. With our model, we qualitatively reproduce the majority of the absorption lines.

We now consider the effect of spectral resolution on the derived column density of neutral hydrogen. Based on the HST medium resolution spectra observed at $\phi = 0.09$, we find $n_{\rm HI} = 1.5 \cdot 10^{24}$ cm^{-2}. A Rayleigh scattered Planck spectrum together with the measured continuum points is shown in Fig. 9. If we convolve the HST spectrum with the IUE resolution, then we fit the spectrum with $0.6 \cdot 10^{24}$ cm^{-2}, together with a wavelength independent attenuation factor $e^{-\tau_A} = 0.3$. Thus the column density of neutral hydrogen derived from an IUE low resolution spectrum, would be underestimated by a factor ≈ 2.5.

6. Discussion

6.1. Mass-loss rate of the M-giant in SY Mus

We are of the opinion that observations of SY Mus are too few to determine the shape of the velocity law of the red giant wind in a unique way. Additional data during egress at $b = 1.5$–2.0 R$_{\rm r}$ would better determine the fit parameter k, and therefore the acceleration region. Nevertheless, we suspect that the wind reaches terminal velocity inside the orbit of the hot companion star. We can then derive the ratio $\dot{M}/v_\infty$. Adopting $v_\infty = 20$ km s^{-1}, we find that egress data indicate a mass-loss rate of $\dot{M} \approx 5 \cdot 10^{-7}$ M$_\odot$/yr. A mass loss rate of $\dot{M} \approx 10^{-7}$ M$_\odot$/yr has been derived with a modified Zanstra method by Mürset et al. (1991). Mass-loss rates of non-variable single M-giants are in the range $\dot{M} \approx 10^{-8} - 10^{-7}$ M$_\odot$/yr (Dupree 1986). The mass-loss rate of the M-giant in SY Mus is thus high compared to its single counterparts. S-type symbiotic binaries are known to have higher 25 μm excess compared to single M-giants (Kenyon et al. 1988). The larger FIR-excess has been interpreted as being due to a higher mass-loss rate.

A mass-loss rate of $\dot{M} \approx 10^{-9}$ M$_\odot$/yr has been derived by Pereira et al. (1999), who also determined a velocity law based on the same IUE observations as used by us. The differences to our result are due to their neglect of the asymmetry of the eclipse curve and the effect of the ionization of hydrogen.

6.2. Possible cause for asymmetric eclipses

In SY Mus the continuum flux attenuation is strongly asymmetric with respect to the mid-eclipse of the white dwarf by the red giant. As the recombination time scales for hydrogen at densities of $10^9 - 10^{10}$ cm^{-3} are too short to produce a significant phase lag of the ionization front, only an asymmetry in the material distribution can lead to the observed asymmetry in the UV-light curve. In their spectropolarimetric data, Harries & Howarth (1996) remarked residual position angle variations, which could be due to an asymmetric red giant wind.

In the following we briefly discuss a scenario which could explain the observed asymmetry.

The hot component in SY Mus has a luminosity of 1 300 L$_\odot$ (Mürset et al. 1991) and $\log g = 6.0$ (Schmutz et al. 1994). For these parameters, the wind momentum-luminosity relation for radiation driven winds of hot stars (Kudritzki 1998) predicts a fast wind. This expectation cannot be verified observationally because IUE high resolution spectra of the stellar continuum of SY Mus are severely under-exposed and therefore too noisy to detect P Cygni profiles. Qualitatively the colliding winds in an s-type symbiotic system, where the orbital motion is comparable to the wind velocity of the red giant, can reproduce the observed variation of the column density around the eclipse. This scenario has already been used by Schild & Schmid (1996) to explain the Raman scattering geometry in V1016 Cyg, which they found to be asymmetric with respect to the binary axis. 3D-hydrodynamical simulations by Walder (1995, 1998) show that, during ingress, the line of sight to the hot star passes through a region which shortly before has been evacuated by the fast wind

from the hot star. The red giant wind is too slow to refill this region. The large pressure gradient from the red giant atmosphere to the evacuated region, produces a strong acceleration of the material ejected by the red giant. This rarefaction wave thus leads to a steep increase of the column density during ingress. The velocity law derived from ingress data does therefore not directly reflect the wind acceleration due to forces from the red giant.

During egress the line of sight to the hot star passes through the region behind the red giant, where shortly before the red giant deposited its wind material. Densities and velocities in the wake of the red giant wind material are less affected by the wind from the hot star. The velocity law derived from egress data is therefore more representative for an undisturbed red giant wind.

The asymmetry between the variation of the column density during ingress and egress is present even if the wind from the hot star momentum is several times smaller than the red giant wind (see Walder 1998).

ROSAT X-ray data (Mürset et al. 1997) and IUE spectra (Vogel 1993) indicate, that the hot component in the eclipsing symbiotic binary EG And has a mass-loss of about $5 \cdot 10^{-9}\,\mathrm{M}_\odot/\mathrm{yr}$, with a terminal velocity of $v_\infty \approx 500\ \mathrm{km\,s^{-1}}$. Therefore it would be interesting to search for asymmetries in the UV light curve of EG And. We have inspected all the available IUE low resolution final archive spectra of EG And. Unfortunately, the egress curve is not well observed, and its steepness cannot be determined. The radial velocity data of EG And also do not allow to derive a precise T_0. The time of conjunction from the radial velocity curve of Munari (1993) is about 30 days ($\Delta\phi = 0.06$) after mid-eclipse according to the UV light curve. The two times are nevertheless consistent as Munari (1993) give an error of 34 days for the time of conjunction. Therefore the available data on EG And do at present not imply any asymmetries in the column density.

6.3. Additional attenuation due to line blanketing

In contrast to SY Mus, RW Hya and BF Cyg, which display continuum attenuation larger than can be accounted for by Rayleigh scattering, the attenuation function in EG And does not differ significantly from the Rayleigh scattering function. In the following we discuss two mechanisms which could lead to reduced line blanketing in EG And.

Because of the high system's velocity of $94.5\ \mathrm{km\,s^{-1}}$ (Munari 1993), EG And is associated with the old population of the Galaxy. EG And thus could have a lower metallicity, resulting in reduced line blanketing. In the available IUE high resolution spectra the continuum is too noisy to detect any absorption lines.

Another possible explanation for reduced line-blanketing can be found in the influence of the electron temperature on atomic level populations. The electron temperature in the red giant wind is dominated by the heating effects due to the companion star. For RW Hya, we found $T_\mathrm{e} \approx 10\,000$ K. According to Mürset et al. (1991) the hot stars in RW Hya and EG And have similar temperatures, but the hot component in EG And is about 25 times less luminous, which implies that the ionization front of hydrogen is farther out in the red giant wind, where densities are smaller. For an estimate, we have calculated the level populations of the material lost by the red giant with an electron temperature, T_e, equal to the red giant temperature $T_\mathrm{eff} \approx 3600$ K. The other parameters given in Sect. 5 were kept unchanged. This electron temperature halves the iron curtain opacity at most wavelengths in the IUE short wavelength range.

Acknowledgements. TD acknowledges financial support from the Swiss National Science Foundation. We thank the night assistants in Garching and La Silla for their continuous support with the ESO CAT observations and the Variable Star Section of the RASNZ for providing us with the electronic record of their visual estimates of SY Mus. We also thank Rolf Walder for fruitful discussions about numerical simulations of colliding winds in symbiotic binaries, and Hans Martin Schmid and Orsola De Marco for giving valuable comments on the manuscript.

References

Dupree A.K., 1986, ARA&A 24, 377
Foster K.W., Wall J., 1998, The Astronomical Almanac
Gonzalez-Riestra R., Cassatella A., Fernandez-Castro T., 1990, A&A 237, 385
Harries T.J., Howarth I.D., 1996, A&A 310, 235
Kenyon S.J., Fernandez-Castro T., Stencel R.E., 1988, AJ 95, 1817
Kenyon S.J., Mikolajewska J., 1995, AJ 110, 391
Knill O., Dgani R., Vogel M., 1993, A&A 274, 1002
Kudritzki R.P., 1998, In: M. Livio (ed.) Proc. of STScI Conference, Cambridge University
Munari U., 1993, A&A 273, 425
Mürset U., Nussbaumer H., Schmid H.M., Vogel M., 1991, A&A 248, 458
Mürset U., Wolff B., Jordan S., 1997, A&A 319, 201
Pereira C.B., Vogel M., Nussbaumer H., 1995, A&A 293, 783
Pereira C.B., Ortega V.G., Monte-Lima I., 1999, A&A 344, 607
Schaller G., Schaerer D., Meynet G., Maeder A., 1992, A&AS 96, 269
Schmid H.M., 1995, MNRAS 275, 227
Schmutz W., Pereira C., Mueller D., 1993, In: Regev O., Shaviv G. (eds.) Cataclysmic Variables and Related Physics. Annals Israel Phys. Soc. 10, Inst. of Physics Publishing, Bristol, p. 311
Schmutz W., Schild H., Mürset U., Schmid H.M., 1994, A&A 288, 819
Schild H., Mürset U., Schmutz W., 1996, A&A 306, 477
Schild H., Schmid H.M., 1996, A&A 310, 211
Schwank M., Schmutz W., Nussbaumer H., 1997, A&A 319, 166
Shore S.N., Aufdenberg J.P., 1993, ApJ 416, 355
Vogel M., 1991, A&A 249, 173
Vogel M., Nussbaumer H., Monier R., 1992, A&A 260, 156
Vogel M., 1993, A&A 274, L21
Walder R., 1995, In: van der Hucht K.A., Williams P.M. (eds.) Proc. IAU Symp. 163, Wolf-Rayet stars: binaries, colliding winds, evolution. p. 420
Walder R., 1998, Ap&SS 260, 243
Zahn J.-P., 1977, A&A 57, 383